



# OPEN Study on the constitutive model and thermal deformation behavior of Incoloy825/P110 bimetallic composite material

Hao Liu<sup>1</sup>, Qiang Li<sup>2</sup>, Hailian Gui<sup>1</sup>✉, Chen Zhang<sup>1</sup>, Sha Li<sup>1</sup>, Leifeng Tuo<sup>1</sup>, Jianxun Chen<sup>1</sup>, Pengyue Zhang<sup>3</sup> & Chunlei Shen<sup>4</sup>

To further investigate the properties of Incoloy825/P110 bimetallic composite seamless pipes, thermal deformation analysis was conducted on their billets. The thermal deformation and dynamic recrystallization (DRX) behavior of Incoloy825/P110 bimetallic composite materials were studied through hot compression tests at deformation temperatures (850–1150 °C) and strain rates (0.01–10 s<sup>-1</sup>). A constitutive relationship was established, and compensation and correction were made based on the differences in materials corresponding to different strain states. The hot processing map was established based on the thermal deformation behavior of bimetallic materials. In addition, the evolution of microstructure was also studied to verify the feasibility of the established hot processing map. The results show that the strain compensated Arrhenius can accurately predict the flow stress. By analyzing the microstructure using EBSD, it can be found that DRX behavior has a significant impact on the thermal processing properties of composite materials. This study provides an important theoretical basis for the production of Incoloy825/P110 bimetallic composite seamless pipes in the future.

**Keywords** Composite materials, Thermal deformation, Hot processing map, Dynamic recrystallization

Bimetallic composite seamless pipe is composed of two different materials of metal pipes, one as the base pipe and the other as the liner pipe, with the base pipe on the outside and the liner pipe on the inside, tightly bonded together through different processes as shown in Fig. 1. In transportation systems such as natural gas and oil, carbon steel with good rigidity, strong pressure bearing capacity, and low cost is usually selected as the material for the base pipe, while stainless steel or nickel-based alloy with corrosion resistance and wear resistance is selected as the material for the liner pipe<sup>1</sup>. The emergence of bimetallic composite seamless pipes has gradually replaced the use of stainless steel, saving the amount of stainless steel used without affecting its use and greatly reducing costs.

Incoloy825 alloy is an alloy with Ni–Fe–Cr as the main alloying element, and added with elements such as Ti, Cu, and Mo. The seamless pipes of this alloy are widely used in various corrosive industrial environments and have high strength and excellent corrosion resistance. Incoloy825 alloy can also maintain its strength at high temperatures and is also a high-temperature alloy<sup>2</sup>. Although it has excellent performance, its manufacturing cost is relatively high. P110 steel has the characteristics of good rigidity, high load-bearing capacity, and low cost, and is commonly used in the production and transportation of seawater. The Incoloy825/P110 bimetallic composite seamless pipe, which is composed of Incoloy825 alloy as the liner and P110 steel as the base pipe, precisely meets the excellent characteristics of both materials.

The hot forming process significantly depends on the nonlinear relationship between the microstructural evolution and deformation parameter<sup>3–5</sup>. The deformation mechanisms such as work hardening (WH), dynamic recovery (DRV), and dynamic recrystallization (DRX) are greatly affected by thermal deformation<sup>6</sup>. In order to investigate the precise control and mechanical properties of bimetallic composite materials during hot forming, it is necessary to conduct a comprehensive analysis of the hot deformation behavior of Incoloy825/P110.

<sup>1</sup>Department of Materials Science and Engineering, Taiyuan University of Sciences and Technology, Taiyuan 030024, People's Republic of China. <sup>2</sup>Department of Intelligent Manufacturing, Shanxi Vocational University of Engineering Science and Technology, Jinzhong 030619, People's Republic of China. <sup>3</sup>Shanxi Steel Heli New Material Technology Co., Ltd, Taiyuan 030021, People's Republic of China. <sup>4</sup>Jiangsu Aegis Haizhu Machinery Co., Ltd, Huaian 223100, People's Republic of China. ✉email: guihailian2000@163.com

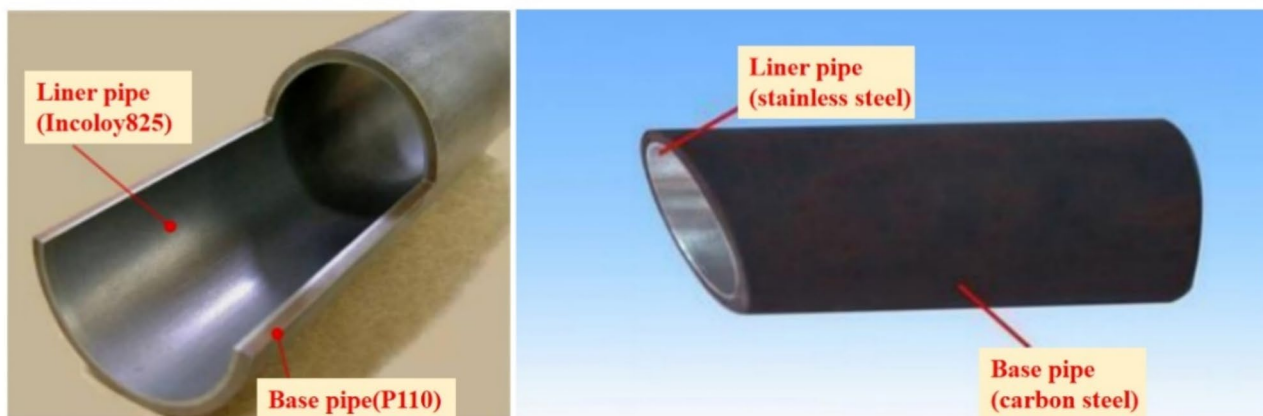


**Fig. 1.** Bimetallic composite seamless pipe.

In recent years, there have been many studies on the hot deformation behavior of nickel based high-temperature alloys. Usually, an accurate constitutive model needs to be constructed first, followed by numerical simulation of the plastic flow behavior during hot forming. The constitutive equation containing coupled deformation parameters effectively supports the numerical simulation of the hot forming process<sup>7,8</sup>. Compared with constitutive models based on physics and artificial neural networks (ANN), empirical models are more intuitive and convenient for characterizing metal materials. Thus, the empirical models, including the Arrhenius constitutive model<sup>9</sup>, Johnson-Cook (JC) constitutive model<sup>10</sup>, Hansel-Spittel constitutive model<sup>11</sup>, Field-Backofen (F-B) model<sup>12</sup>, and Khan-Huang-Liang (KHL) model<sup>13</sup>, have been widely applied to examine the hot deformation behavior of different alloys. Geng et al.<sup>14</sup> reproduced the relationship between the true stress and true strain of GH4169 superalloy by using the F-B, JC, and Arrhenius models. The results indicate that the Arrhenius model has the highest accuracy among the three models. Song<sup>15</sup>, Zhao et al.<sup>16–20</sup> developed various constitutive equations to describe the relationships between parameters such as stress, strain, temperature, and strain rate during thermal deformation, and analyzed them. The hot processing map based on dynamic material model (DMM) is commonly used to predict the deformation mechanism and microstructure characteristics of materials under different deformation conditions, which can provide valuable guidance for material processing<sup>21</sup>.

Hot processing map is an effective tool for evaluating the hot workability of various metal materials<sup>22</sup>. Tian et al.<sup>23</sup> constructed a hot working diagram of Incoloy825 alloy, which provides some guidance for mass production, but neglects its material cost. Kong et al.<sup>24</sup> investigated the hot tensile behavior of Incoloy625 high-temperature alloy sheet and optimized the hot working parameters based on DMM. However, they did not provide a detailed description of the dynamic microscale mechanisms involved. Chi et al.<sup>25</sup> studied the hot compression deformation process of powder metallurgy high-temperature alloys, but did not further optimize the processing parameters, which may result in cracks appearing at the hot processing window. Zhu et al.<sup>26</sup> used an ANN model to establish a three-dimensional (3D) hot working map of alloy 925 high-temperature alloy. Although it alleviates the lack of experimental data, it is not suitable for practical working conditions in complex environments. In addition, the hot workability zones of alloys such as Ti–47.5Al–2.5V–1.0Cr–0.2Zr<sup>27</sup>, Incoloy718 high-temperature alloy<sup>28</sup>, and martensitic stainless steel<sup>29</sup> were explored. Phenomena in alloy materials, such as point defect recombination at symmetrically tilted grain boundaries<sup>30</sup>, the distribution of atomic energies and activation barriers<sup>31</sup>, as well as various fine structures, nanotwins, and homogeneous amorphous regions<sup>32,33</sup>, all require analysis under specific constrained conditions.

This study conducted hot compression tests on Incoloy825/P110 bimetallic composite materials to investigate their thermal deformation behavior within the processing temperature range of 850–1150 °C and strain rate of 0.01–10 s<sup>-1</sup>. The constitutive model with strain compensation and correction was constructed, and a hot processing map based on DMM was drawn to describe its rheological and thermal processing characteristics. The microstructure evolution and DRX mechanism at different temperatures were studied using electron backscatter diffraction (EBSD) data.

## Materials and experiments

The experiment used a self-made gravity based solid-liquid composite pipe billet production device to produce Incoloy825/P110 bimetallic composite pipe billets, as shown in Fig. 2a, and their chemical composition is shown in Table 1. Figure 2b shows the metallographic structure of Incoloy825 high-temperature alloy, with a large equiaxed austenite structure. Figure 2c shows that the metallographic structure of P110 is mainly composed of ferrite. A metallurgical bond is formed between Incoloy825 and P110, which has high interfacial toughness and is not easily cracked. Cut a cylindrical sample from the bar material using wire cutting, and then polish the two end faces and outer surface with a grinder. The sample size is  $\Phi 8 \times 12$  mm. In order to maintain the same initial microstructure before thermal deformation of the samples, the same batch of cast bars were taken for all samples.

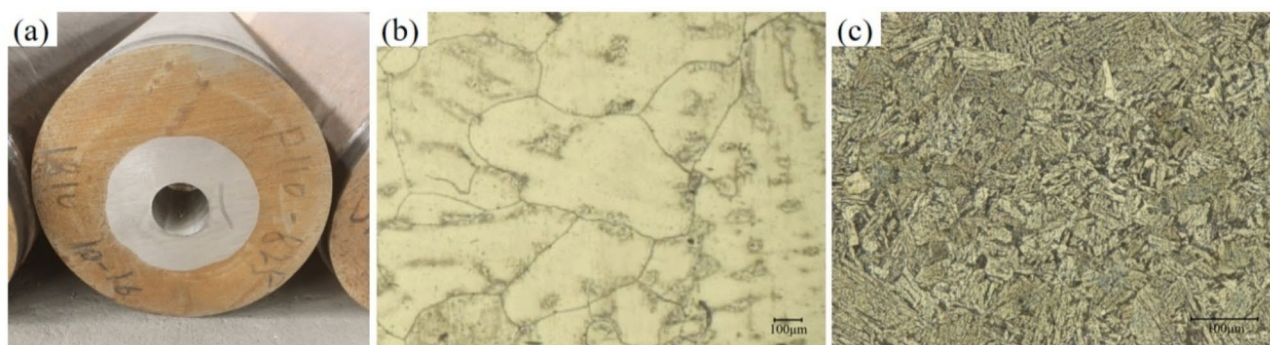


**Fig. 2.** The initial bimetallic tube blank: (a) Incoloy825/P110 composite pipe blank, (b) Microstructure of Incoloy825, (c) Microstructure of P110.

Component	Ni	Fe	Cr	Mo	C	Mn	Si
Incoloy825	45.4	27.2	22.5	2.5	1.3	0.7	0.4
P110 steel	0	96.4	1.0	0.7	1.1	0.5	0.3

**Table 1.** Chemical composition of Incoloy825/P110 bimetallic composite materials (wt%).

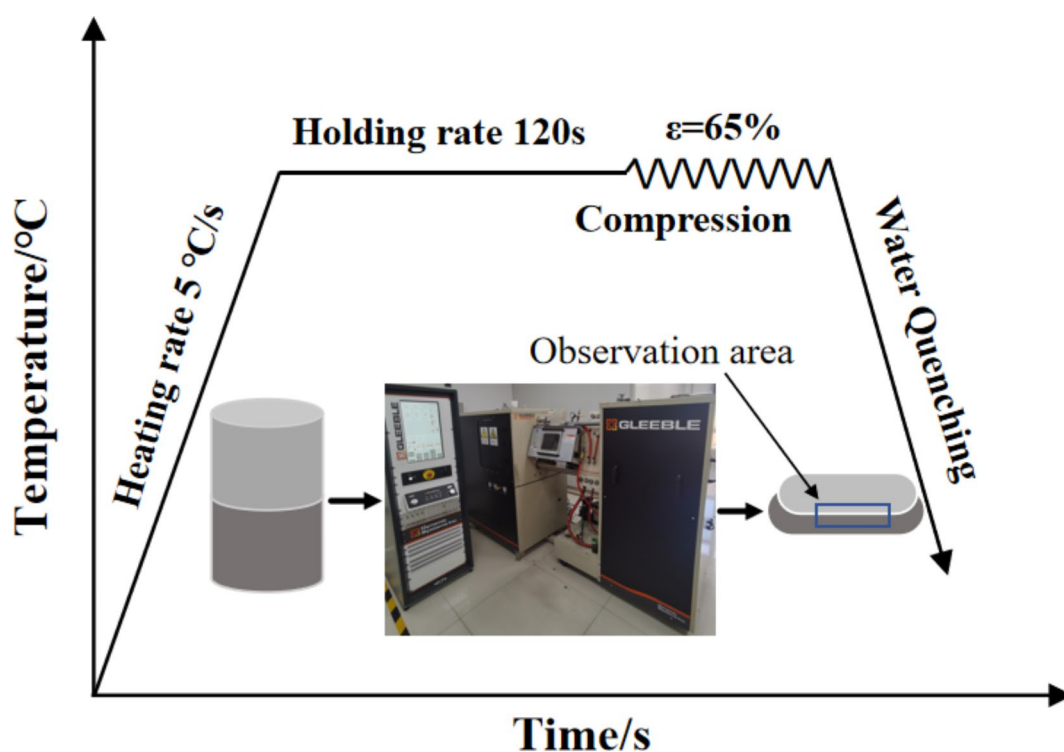


**Fig. 3.** Schematic of Incoloy825/P110 bimetallic composite materials hot compression test.

Perform thermal compression test on a thermal simulation tester (Gleeble-3800). The schematic diagram of the experimental process shown in Fig. 3. In order to reduce the friction between the sample and the mold, tantalum slices with a thickness of 0.1 mm were placed on both ends of the sample. Firstly, the samples were heated to the predesigned temperature at a rate of 5 °C/s, and the temperature was kept for 120 s to homogenize the microstructure. Then, they were heated to compression temperatures of 850 °C, 950 °C, 1050 °C and 1150 °C with 0.01 s<sup>-1</sup>, 0.1 s<sup>-1</sup>, 1 s<sup>-1</sup> and 10 s<sup>-1</sup> strain rates, respectively. The sample was compressed to 65% of its initial height, and the experiment was terminated. To maintain the high-temperature microstructure, the sample was quenched in water. The compressed samples were cut along the central axis using a wire cutting machine. After sandpaper and mechanical polishing, the samples were electrochemically polished with a mixture of 10%

perchloric acid and 90% anhydrous ethanol at 25 V for 70 s. The EBSD microstructures were investigated using a scanning electron microscope (FEI Nova Nano SEM 450). Finally, the EBSD data were post-processed using OIM software (version of 7.2).

## Results and discussion

### Flow behavior

Figure 4 shows the stress-strain curves of Incoloy825/P110 bimetallic composite material under deformation at different temperatures. From the figure, it can be seen that the rheological curve morphology of Incoloy825/P110 bimetallic composite material remains similar during the hot compression process at different deformation temperatures and deformation rates. During the initial deformation stage, the bimetallic material changes from its original shape into a compressed form. The pressure provided by the experimental simulator causes a sharp increase in the dislocation density inside the material, with the main deformation mechanism being WH. Therefore, there is a trend of rapid increase in flow stress, and higher stress levels can be achieved at lower deformation amounts. With the accumulation of deformation, the softening mechanism within the alloy also increases, accompanied by DRV, DRX, and WH phenomena. However, WH still dominates, and the level of stress increase gradually slows down and reaches its peak. When the hot compression deformation reaches a certain value, the effect of the softening mechanism will further expand, combined with the WH during the deformation process to achieve a dynamic equilibrium state, gradually stabilizing the stress value.

At the same time, the rheological curve is not smooth at strain rates of  $0.01\text{ s}^{-1}$ ,  $0.1\text{ s}^{-1}$  and  $1\text{ s}^{-1}$ , and the stress exhibits a serrated phenomenon. On the one hand, it is caused by dynamic strain aging (DSA). On the other hand, due to the low deformation rate or high deformation temperature, the increase rate of dislocation density is relatively small. After dynamic recrystallization, further work hardening is necessary before recrystallization nucleation can occur again. As the mechanisms of work hardening and softening alternate and compete fiercely, flow stress may also exhibit serrated shapes.

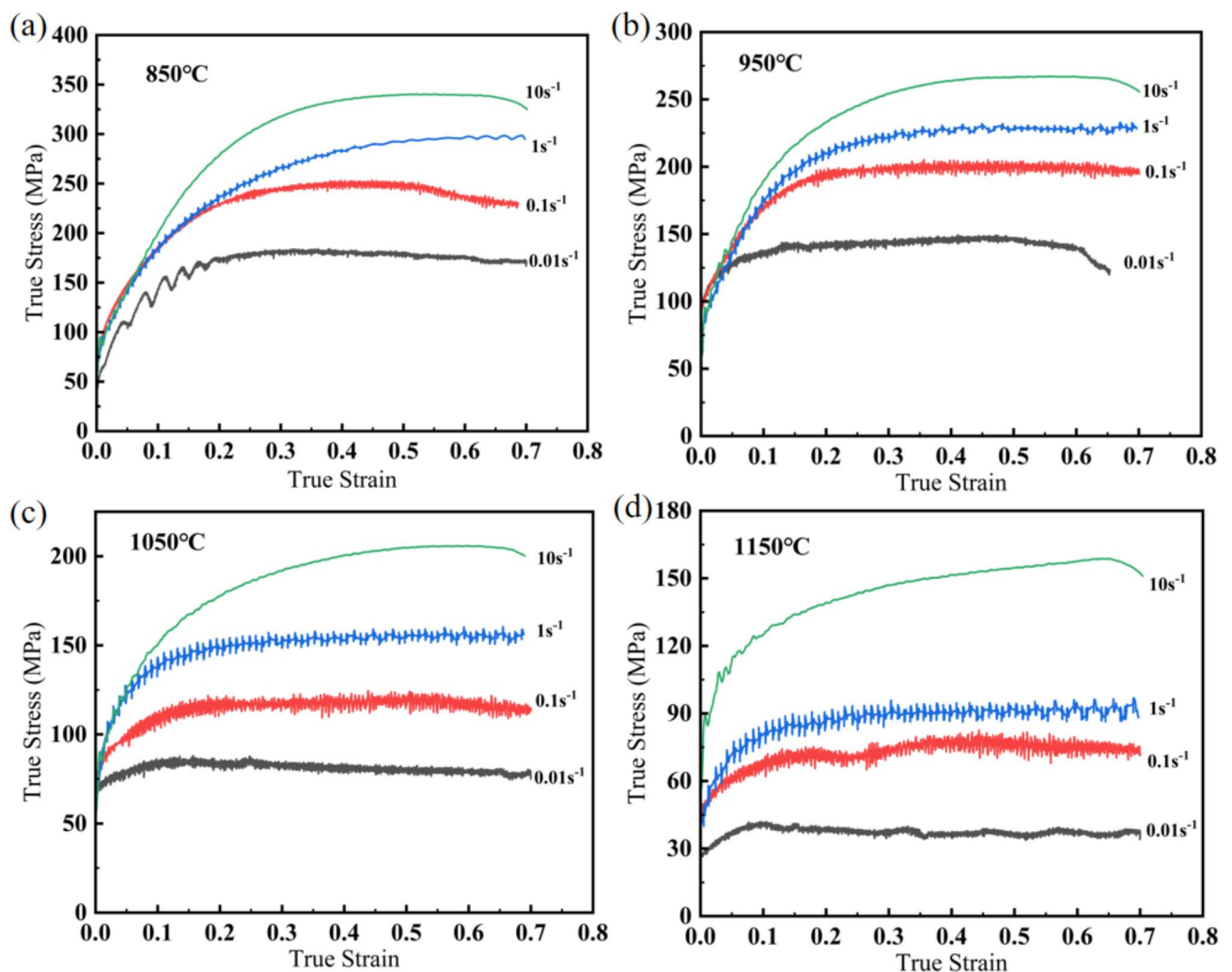


**Fig. 4.** True stress–strain curves of 825/P110 bimetallic deformation at different temperatures: (a) 850 °C, (b) 950 °C, (c) 1050 °C, (d) 1150 °C.

In the hot compression deformation of Incoloy825/P110 bimetallic composite material, the corresponding rheological stress values are the highest at a deformation rate of  $10 \text{ s}^{-1}$ , which are 341 MPa, 267 MPa, 206 MPa, and 160 MPa, respectively. The rheological stress values corresponding to a deformation rate of  $0.01 \text{ s}^{-1}$  are the smallest, which are 185 MPa, 151 MPa, 90 MPa, and 42 MPa, respectively, followed by  $0.1 \text{ s}^{-1}$  and  $1 \text{ s}^{-1}$  from small to large. At a constant strain rate, as the true strain increases, the stress values on the curve at each temperature gradually increase. Taking the stress-strain curve at  $1050 \text{ }^\circ\text{C}$  and a strain rate of  $0.01 \text{ s}^{-1}$  as an example, it can be observed that the stress-strain curve can be divided into three stages. In the first stage, when the loading strain is less than the critical strain for DRX of 0.1, the WH effect due to dislocation proliferation exceeds the softening effect caused by DRV. As a result, the stress-strain curve shows a trend of rapid increase in rheological stress. In the second stage, when the loading strain is between 0.1 and 0.15, the rheological stress gradually increases to the peak stress of 90 MPa. In this stage, due to the loading strain exceeding the critical strain for DRX, the composite material undergoes DRX. The softening effect from this process is significantly greater than the DRX, leading to a noticeable slowing in the rate of increase of rheological stress. In the third stage, when the loading strain exceeds the peak strain of 0.15, the dynamic softening effects (DRX and DRV) become greater than the WH effect. As a result, the rheological stress decreases with increasing strain. Finally, the rheological curve reaches and maintains a stable state, achieving dynamic equilibrium. In addition, the curve at  $1150 \text{ }^\circ\text{C}$  and strain rate of  $10 \text{ s}^{-1}$  does not exhibit typical DRX softening characteristics. This is due to the rapid generation and proliferation of dislocations during hot compressive deformation at high strain rates, where the softening effects from DRV and DRX are insufficient to offset the WH effect. As a result, the stress-strain curve exhibits a monotonically increasing trend. When the deformation temperature of composite material changes, the stress value fluctuates greatly. Taking a strain rate of  $1 \text{ s}^{-1}$  as an example, as the temperature increases from  $850 \text{ }^\circ\text{C}$  to  $1150 \text{ }^\circ\text{C}$ , the rheological stresses are 300 MPa, 225 MPa, 155 MPa, and 90 MPa, respectively. When the deformation rate is constant, the higher the deformation temperature, the greater the decrease in rheological stress. It is because when the deformation temperature of composite materials is high, the internal dislocation density decreases, and the degree of WH decreases, and at the same time, the shear stress required for dislocations and slip decreases, making plastic deformation easier.

Figure 5a shows the effect of deformation temperature on peak stress in Incoloy825/P110 bimetallic composite material. When the deformation temperature of composite materials changes, the stress value fluctuates within a large range. When the deformation rate is  $10 \text{ s}^{-1}$ , the peak stress decreases from 345 MPa to 170 MPa. When the deformation rate is  $1 \text{ s}^{-1}$ , the peak stress decreases from 300 MPa to 105 MPa. When the deformation rate is  $0.1 \text{ s}^{-1}$ , the peak stress decreases from 255 MPa to 90 MPa. When the deformation rate is  $0.01 \text{ s}^{-1}$ , the peak stress decreases from 185 MPa to 35 MPa. So, during hot processing, the pressure required for processing will decrease with the increase of material temperature. When the deformation temperature of the alloy is high, the internal dislocation density of the bimetallic alloy decreases, and the degree of work hardening decreases. At the same time, the shear stress required for dislocations and slip decreases, making plastic deformation easier. The difficulty of DRX during the compression process at  $850 \text{ }^\circ\text{C}$  and  $950 \text{ }^\circ\text{C}$  is greater, resulting in a large number of dislocations to form substructure organization, resulting in obvious WH, and the higher the energy required to overcome the pinning effect.

As shown in Fig. 5b, comparing the effects of deformation rate and peak stress, it can be seen that the lower the compression rate, the longer the time required to complete deformation. The softening mechanism plays a strong role in this process, keeping the entire deformation process at a low stress level. If the deformation rate increases, the WH effect is enhanced, and the time for dislocation slip and climb to occur inside the material is

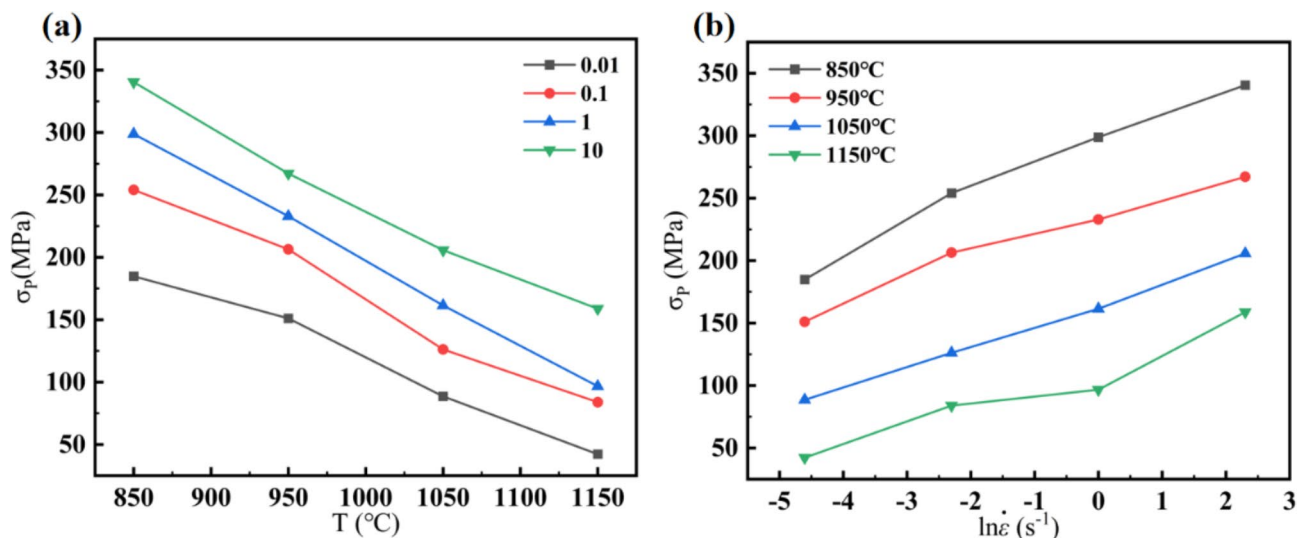


**Fig. 5.** The effect of deformation temperature and deformation rate on peak stress: (a) deformation temperature, (b) deformation rate.

shortened, which weakens the softening effect to a certain extent and leads to insufficient softening behaviors such as DRV and DRX. So, at high strain rates, the material exhibits higher stress levels.

## Modeling of constitutive relationship

### Arrhenius modeling

The Arrhenius-type constitutive equation is extensively employed for elucidating the influence of deformation temperature and strain rate on stress during thermal deformation processes<sup>34</sup>.

$$\begin{cases} \dot{\epsilon} = Af(\sigma) \exp\left(-\frac{Q}{RT}\right) \\ f(\sigma) = \begin{cases} \sigma^{n_1}, & \alpha\sigma < 0.8 \\ \exp(\beta\sigma), & \alpha\sigma > 1.2 \\ [\sinh(\alpha\sigma)]^n, & \text{for all } \sigma \end{cases} \end{cases} \quad (1)$$

where  $\dot{\epsilon}$  is true strain rate ( $s^{-1}$ ),  $Q$  is deformation activation energy (J/mol),  $\sigma$  is true stress (MPa),  $T$  is temperature (K),  $R$  is universal gas constant of 8.314 J/(mol K),  $\alpha$ ,  $n_1$ ,  $\beta$ ,  $n$  and  $A$  are material constants. The stress exponent  $\alpha$  in Eq. (1) can be calculated as  $\alpha = n_1/\beta$ . When  $\alpha\sigma < 0.8$ , it is a low stress level, and when  $\alpha\sigma > 1.2$ , it is a high stress level. The hyperbolic sine law applies to all ranges of stress levels. It is obvious that the effect of strain on flow stress is not considered in Eq. (1). The deriving methods of material constants have been illustrated in previous studies<sup>35,36</sup>.

According to Zener and Hollomon's proposal<sup>37</sup>, the relationship between strain rate and deformation temperature during high-temperature plastic deformation of metal materials can be expressed as:

$$Z = \dot{\epsilon} \exp\left[\frac{Q}{RT}\right] = A [\sinh(\alpha\sigma)]^n \quad (2)$$

Taking the logarithm on both sides yields:

$$\ln Z = \ln \dot{\epsilon} + \frac{Q}{RT} = \ln A + n \ln [\sinh(\alpha\sigma)] \quad (3)$$

In the hot compression simulation experiment, the  $\dot{\epsilon}$  and strain activation energy  $Q$  at different temperatures were used to calculate  $\ln Z$ , as shown in Table 2. Fit the  $\ln [\sinh(\alpha\sigma)] - \ln Z$  linear relationship of composite materials at different temperatures and strain rates, and the linear fitting effect is good. The intercept of the diagonal line is  $\ln A = 40.09$ . Therefore, the structural factor  $A = 2.58 \times 10^{17}$ .

Obtain the constitutive model of Incoloy825/P110 bimetallic composite material in different temperature ranges:

$$\dot{\epsilon} = 2.58 \times 10^{17} [\sinh(0.006\sigma_p)]^{6.7929} \exp\left(-\frac{445484}{RT}\right) \quad (4)$$

The constitutive model of high-temperature deformation flow stress in composite materials is described using the Zener-Hollomon parameter as follows:

$$Z = \dot{\epsilon} \exp\left(\frac{445484}{RT}\right) = 2.58 \times 10^{17} [\sinh(0.006\sigma)]^{6.7929} \quad (5)$$

Number	$\dot{\epsilon}/s^{-1}$	T (K)	$\ln Z$	$\ln \sinh(\alpha\sigma_p)$
1	0.01	1123	43.108	0.30188
2	0.1		45.411	0.78224
3	1		47.714	1.07281
4	10		50.016	1.33601
5	0.01	1223	39.207	0.03453
6	0.1		41.510	0.46176
7	1		43.812	0.64186
8	10		46.115	0.86741
9	0.01	1323	35.895	-0.58028
10	0.1		38.198	-0.18621
11	1		40.501	0.12438
12	10		42.803	0.45466
13	0.01	1423	33.049	-1.36776
14	0.1		35.352	-0.64320
15	1		37.655	-0.48545
16	10		39.957	0.10024

**Table 2.** The parameters corresponding to different temperatures and strain rates.

### Compensation and correction of the model

Changes in strain can also cause changes in the stress values of the rheological curve. The construction of the above constitutive equation is calculated by substituting peak values, ignoring the influence of stress variables on stress values, so the materials corresponding to different strain states may vary.

$$\sinh^{-1}(\alpha\sigma) = \ln \left\{ \alpha\sigma + [(\alpha\sigma)^2 + 1]^{\frac{1}{2}} \right\} \quad (6)$$

Combining formulas (1) and (2), the flow stress can be expressed as,

$$\sigma = \frac{1}{\alpha} \ln \left\{ \left[ \frac{\dot{\epsilon} \exp\left(\frac{Q}{RT}\right)}{A} \right]^{\frac{1}{n}} + \left[ \left( \frac{\dot{\epsilon} \exp\left(\frac{Q}{RT}\right)}{A} \right)^{\frac{2}{n}} + 1 \right]^{\frac{1}{2}} \right\} \quad (7)$$

To improve the accuracy of prediction, the influence of strain on material constants should be considered. Therefore, a fifth order polynomial function is used to describe the relationship between strain ( $\epsilon$ ) and material constants  $\alpha$ ,  $n$ ,  $Q$ ,  $A$ :

$$\begin{cases} \alpha = B_0 + B_1\epsilon + B_2\epsilon^2 + B_3\epsilon^3 + B_4\epsilon^4 + B_5\epsilon^5 \\ n = C_0 + C_1\epsilon + C_2\epsilon^2 + C_3\epsilon^3 + C_4\epsilon^4 + C_5\epsilon^5 \\ Q = D_0 + D_1\epsilon + D_2\epsilon^2 + D_3\epsilon^3 + D_4\epsilon^4 + D_5\epsilon^5 \\ \ln A = E_0 + E_1\epsilon + E_2\epsilon^2 + E_3\epsilon^3 + E_4\epsilon^4 + E_5\epsilon^5 \end{cases} \quad (8)$$

The relationship between strain and material constants is shown in Fig. 6. Table 3 lists the coefficients of the fifth order polynomial fitting curves for  $\alpha$ ,  $n$ ,  $Q$  and  $A$ . Therefore, the flow stress can be predicted based on Eqs. (7), (8), as well as Table 3.

To verify the accuracy of the Arrhenius equation for strain compensation of Incoloy825/P110 bimetallic composite materials, the correlation coefficient ( $R$ ) and average relative error (AARE) were calculated based on Eqs. (9) and (10).

$$R = \frac{\sum_{i=1}^n (E_i - \bar{E})(P_i - \bar{P})}{\sqrt{\sum_{i=1}^n (E_i - \bar{E})^2 \cdot \sum_{i=1}^n (P_i - \bar{P})^2}} \quad (9)$$

$$AARE = \frac{1}{N} \sum_{i=1}^N \left| \frac{E_i - P_i}{E_i} \right| \times 100\% \quad (10)$$

Where  $E_i$  and  $P_i$  represent the experimental values of hot compression and the theoretical formula predicted values of the model,  $\bar{E}$  and  $\bar{P}$  are the mean values of them. As shown in Fig. 7, the comparison between experimental test data and theoretical prediction data. There is a certain error between the experimental values and the theoretical predicted values, but the distribution of each point is relatively uniform.  $R$  and AARE are 0.9801 and 4.94%, respectively.

This indicates that the constructed Arrhenius equation has high prediction accuracy. Therefore, the strain compensated Arrhenius model is suitable for describing the flow stress of Incoloy825/P110 bimetallic composite materials at elevated temperature.

### Hot processing maps

According to DMM<sup>38</sup>, the hot processing map is drawn by superimposing the power dissipation diagram and the instability diagram. It can reflect the regular changes in the microstructure evolution, rheological instability, and thermal workability of the material's deformation temperature and deformation rate. This model considers the plastic deformation material during the hot working process as an independent energy dissipation system. The energy exerted by the external environment on Incoloy825/P110 bimetallic composite materials during deformation can be applied in two aspects. Part of it is the energy  $G$  consumed when bimetallic materials undergo plastic deformation. The other part is the energy  $J$  consumed during the microstructure evolution of bimetallic composite materials, which is calculated as follows:

$$P = \sigma \dot{\epsilon} = G + J = \int_0^{\dot{\epsilon}} \sigma d\dot{\epsilon} + \int_0^{\sigma} \dot{\epsilon} d\sigma \quad (11)$$

When the deformation amount and deformation temperature are constant, the instantaneous distribution ratio of the two types of energy consumption can be represented by the strain rate sensitivity coefficient  $m$ , and the formula is as follows:

$$m = \frac{\partial J}{\partial G} = \frac{\dot{\epsilon} \partial \sigma}{\sigma \partial \dot{\epsilon}} = \frac{\partial \ln \sigma}{\partial \ln \dot{\epsilon}} \quad (12)$$

Usually, the relationship between strain rate and rheological stress can be expressed by a power law equation<sup>39</sup>:

$$\sigma = K \dot{\epsilon}^m \quad (13)$$

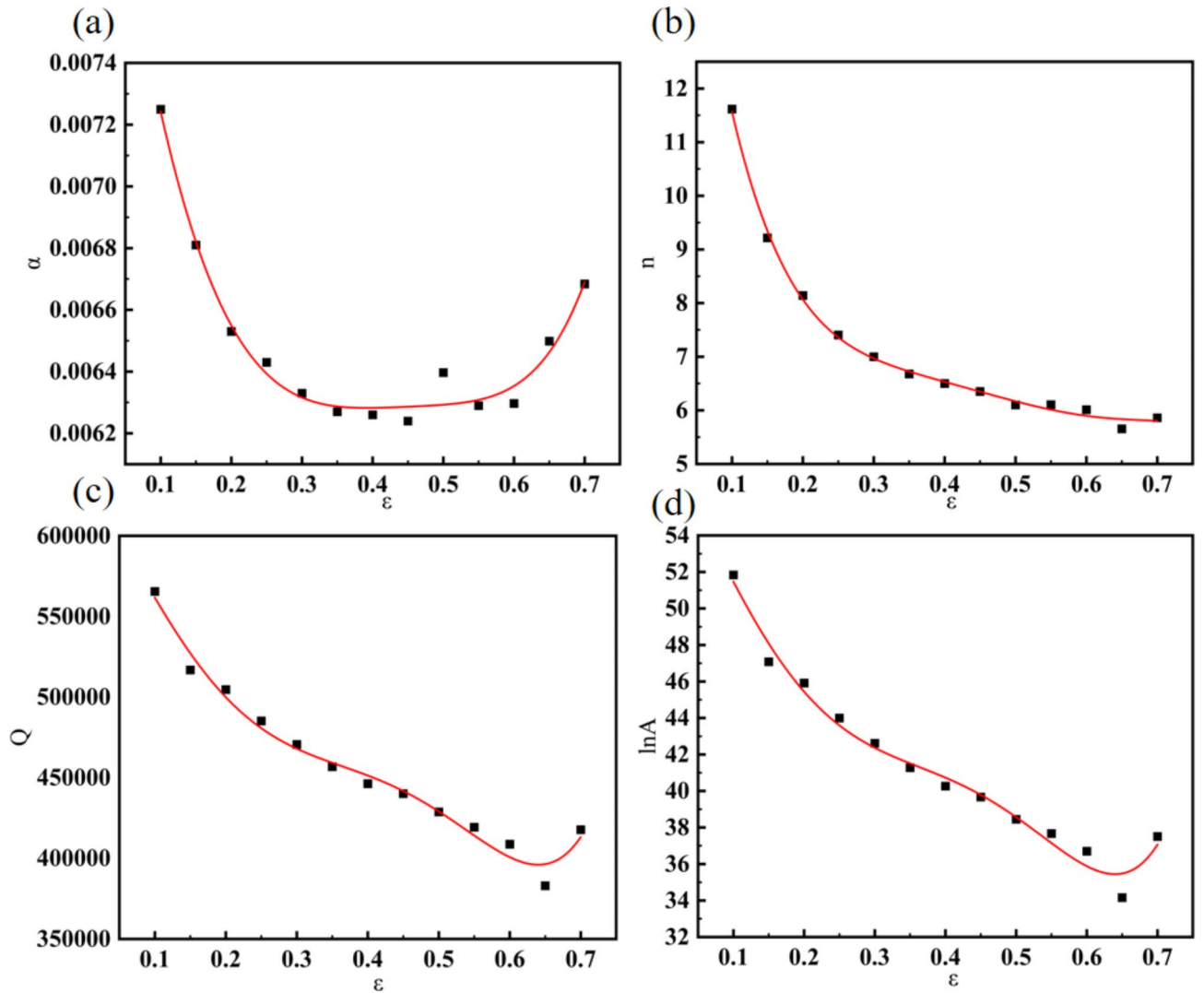


**Fig. 6.** The fifth order fitting curve of Incoloy825-P110 constant and strain; (a)  $\epsilon$ - $\alpha$  curve; (b)  $\epsilon$ - $n$  curve; (c)  $\epsilon$ - $Q$  curve; (d)  $\epsilon$ - $\ln A$  curve.

$\alpha$	$n$	$Q$	$\ln A$
$B_0$ 0.0087	$C_0$ 20.8997	$D_0$ 634,615.2098	$E_0$ 59.0904
$B_1$ -0.0194	$C_1$ -139.19264	$D_1$ -584,726.5943	$E_1$ -67.5347
$B_2$ 0.0533	$C_2$ 562.98708	$D_2$ -3,022,702.3961	$E_2$ -220.9918
$B_3$ -0.0455	$C_3$ -1152.05116	$D_3$ 1.9253E7	$E_3$ 1649.9565
$B_4$ -0.0294	$C_4$ 1155.6578	$D_4$ -3.6207E7	$E_4$ -3211.6824
$B_5$ 0.0485	$C_5$ -451.27	$D_5$ 2.2363E7	$E_5$ 2015.3846

**Table 3.** The coefficients of five order polynomial function.

Based on Eqs. (11) and (13), there is,

$$J = \int_0^{\sigma} \dot{\epsilon} d\sigma = \frac{m}{m+1} \sigma \dot{\epsilon} = \frac{m}{m+1} P \tag{14}$$

For steady-state rheological stress, when  $0 < m < 1$ , the bimetallic composite material is in a nonlinear dissipative state; When  $m = 1$ , the material approaches the ideal linear dissipation state,  $J_{max} = \sigma \dot{\epsilon} / 2 = P / 2$ . The power dissipation characteristics of the microstructure evolution of bimetallic composite materials during plastic

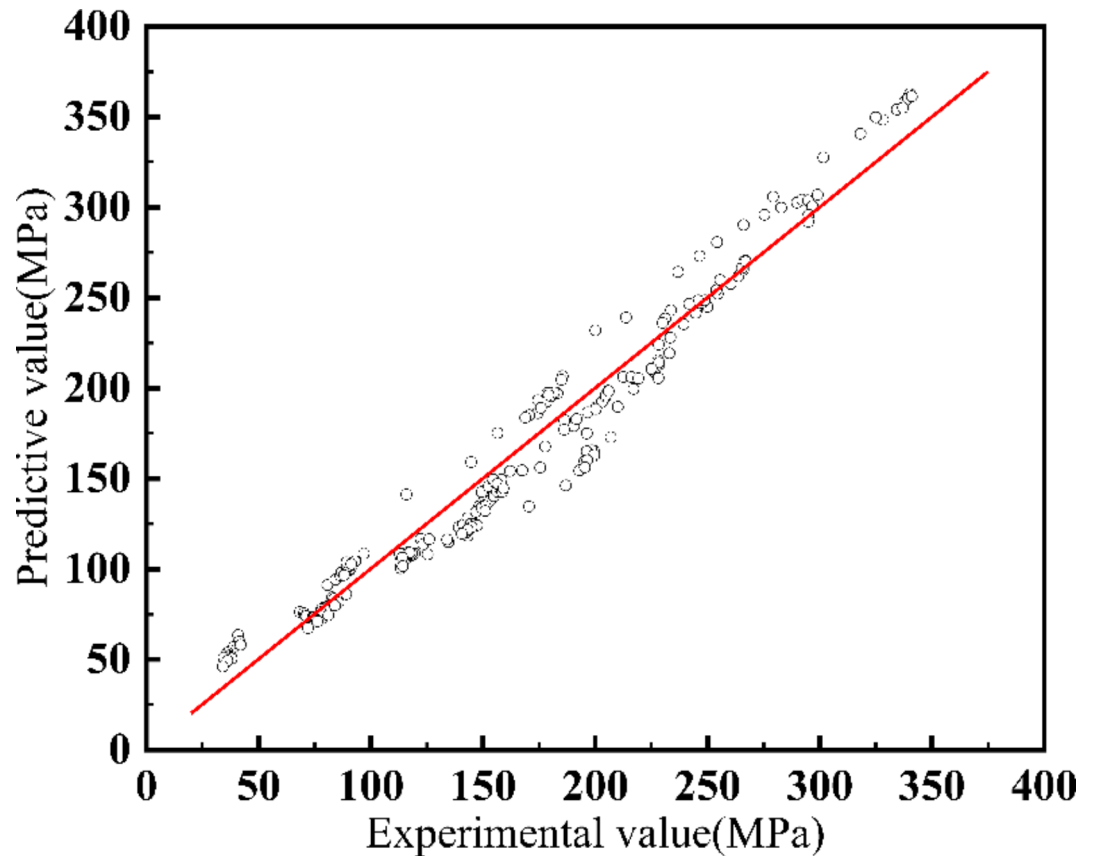


Fig. 7. Correlation between the experimental and predicted flow stress.

deformation can be calculated using the power dissipation coefficient  $\eta$  as the proportion of  $J$ , and the formula can be derived as follows:

$$\eta = \frac{J}{J_{max}} = \frac{2m}{m+1} \quad (15)$$

Usually, materials with high power dissipation have good processability. However, high dissipation areas cannot fully represent the optimal processing area. Sometimes, flow instability may occur in this region. According to the instability criterion<sup>40,41</sup>, the instability coefficient  $\xi(\dot{\epsilon})$  is defined as:

$$\xi(\dot{\epsilon}) = \frac{\partial \ln\left[\frac{m}{m+1}\right]}{\partial \ln \dot{\epsilon}} + m \quad (16)$$

In Eq. (16), if  $\xi(\dot{\epsilon}) > 0$ , it can be considered as a machinable area. If  $\xi(\dot{\epsilon}) < 0$ , it can be considered that flow instability phenomena such as thermal cracking and local shear are prone to occur, and should be avoided during hot processing. Thus, the regions where  $\xi(\dot{\epsilon}) > 0$  and have high  $\eta$  values are identified as the optimal processing ranges on the hot working map. Furthermore, by utilizing more appropriate hot deformation rates and temperature ranges, this can guide actual production practices.

Based on the above principle, using cubic spline curves to fit  $\ln \dot{\epsilon}$  and  $\ln \sigma$  according to the hot compression test data, the values of  $a$ ,  $b$ ,  $c$ , and  $d$  can be obtained through regression, as follows:

$$\ln \sigma = a + b(\ln \dot{\epsilon}) + c(\ln \dot{\epsilon})^2 + d(\ln \dot{\epsilon})^3 \quad (17)$$

By taking the partial derivative of the above formula, the strain rate sensitivity coefficient  $m$  can be obtained as:

$$m = \frac{d \ln \sigma}{d \ln \dot{\epsilon}} = b + 2c(\ln \dot{\epsilon}) + 3d(\ln \dot{\epsilon})^2 \quad (18)$$

Obtain the values of  $m$  and  $\eta$  using formulas (15) and (18). The sensitivity coefficient  $m$  of strain rate is affected by different strain rates and temperatures. A three-dimensional graph of  $m$  is plotted with  $T$  and  $\ln \dot{\epsilon}$  as coordinates, as shown in Fig. 8. Irregular changes in  $m$  caused by non-basal slip and complex deformation under different conditions.

Similarly, for solving the instability factor, plot the  $\ln \dot{\epsilon} - \ln[m/(m+1)]$  relationship and fit a cubic polynomial as follows:

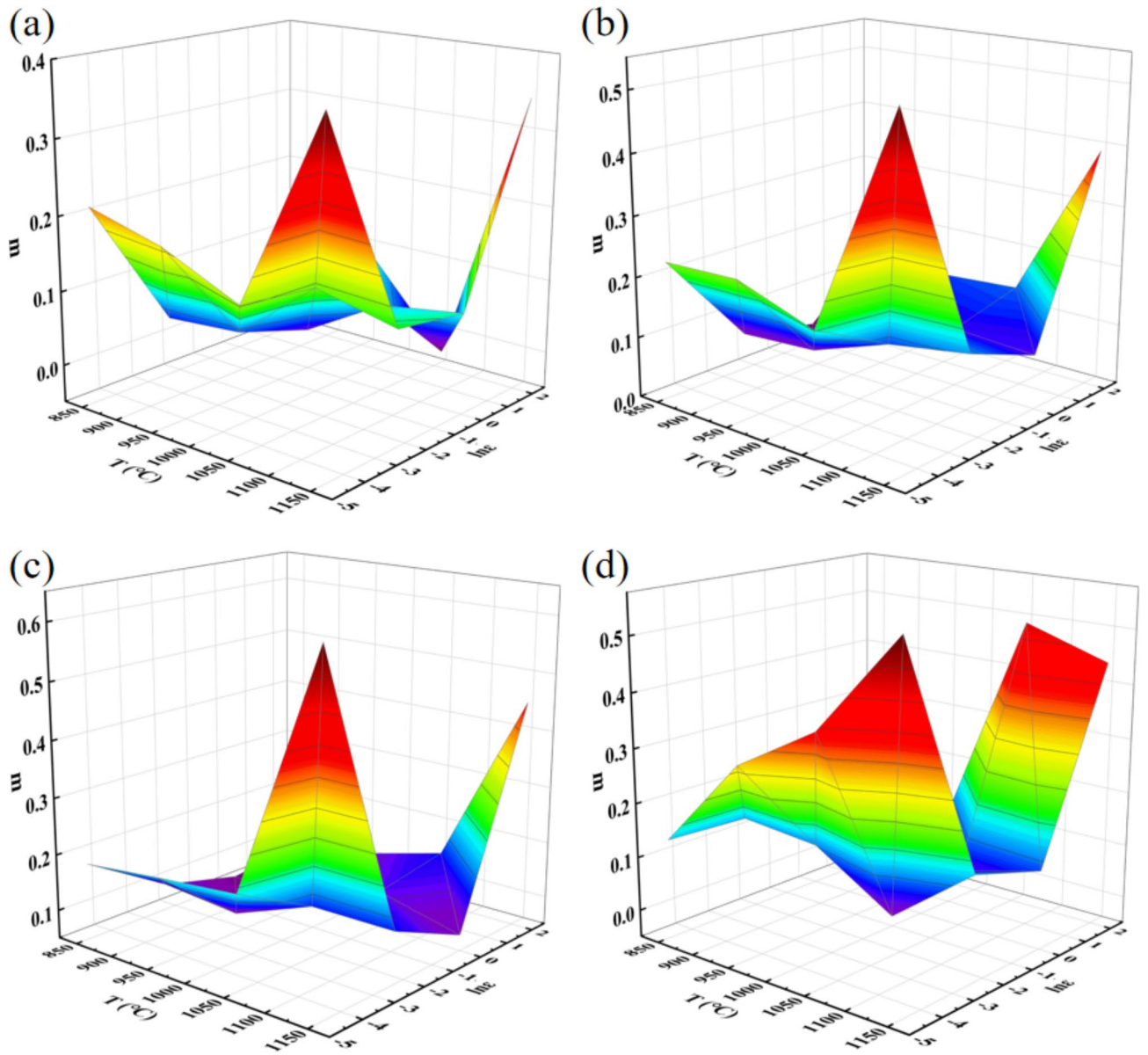


**Fig. 8.** 3D surface plots of Incoloy825/P110 bimetallic composites at the strain of: (a) 0.1; (b) 0.3; (c) 0.5; (d) 0.7.

$$\ln \frac{m}{m+1} = e + f (\ln \dot{\epsilon}) + g (\ln \dot{\epsilon})^2 + h (\ln \dot{\epsilon})^3 \tag{19}$$

Obtain the values of the corresponding coefficients e, f, g, and h through the relationship diagram, calculate the partial derivative of the above equation and combine it with Eq. (16) to derive:

$$\xi(\dot{\epsilon}) = f + 2g (\ln \dot{\epsilon}) + 3h (\ln \dot{\epsilon})^2 + m \tag{20}$$

According to different deformation conditions, the energy dissipation diagram and rheological instability diagram with temperature T as the horizontal axis and strain rate  $\ln \dot{\epsilon}$  as the vertical axis are superimposed to construct the hot processing maps of Incoloy825/P110 bimetallic composite material, with strain variables of 0.1, 0.3, 0.5, and 0.7, as shown in Fig. 9.

The shaded gray area represents the processing instability zone during thermoplastic processing, while the white area represents the machinable zone during thermoplastic processing. The value on the contour line is the energy dissipation factor  $\eta$ , and the  $\eta$  in the machinable zone gradually increases with the increase of temperature, with its peak located in the high-temperature zone. The value of  $\eta$  generally increases with the increase of strain. The degree of DRX increases with the increase of strain, and the evolution of microstructure requires more energy. So, in the process of thermal deformation, the higher the energy dissipation rate, the greater the proportion of microstructural evolution, and the increase in  $\eta$ .

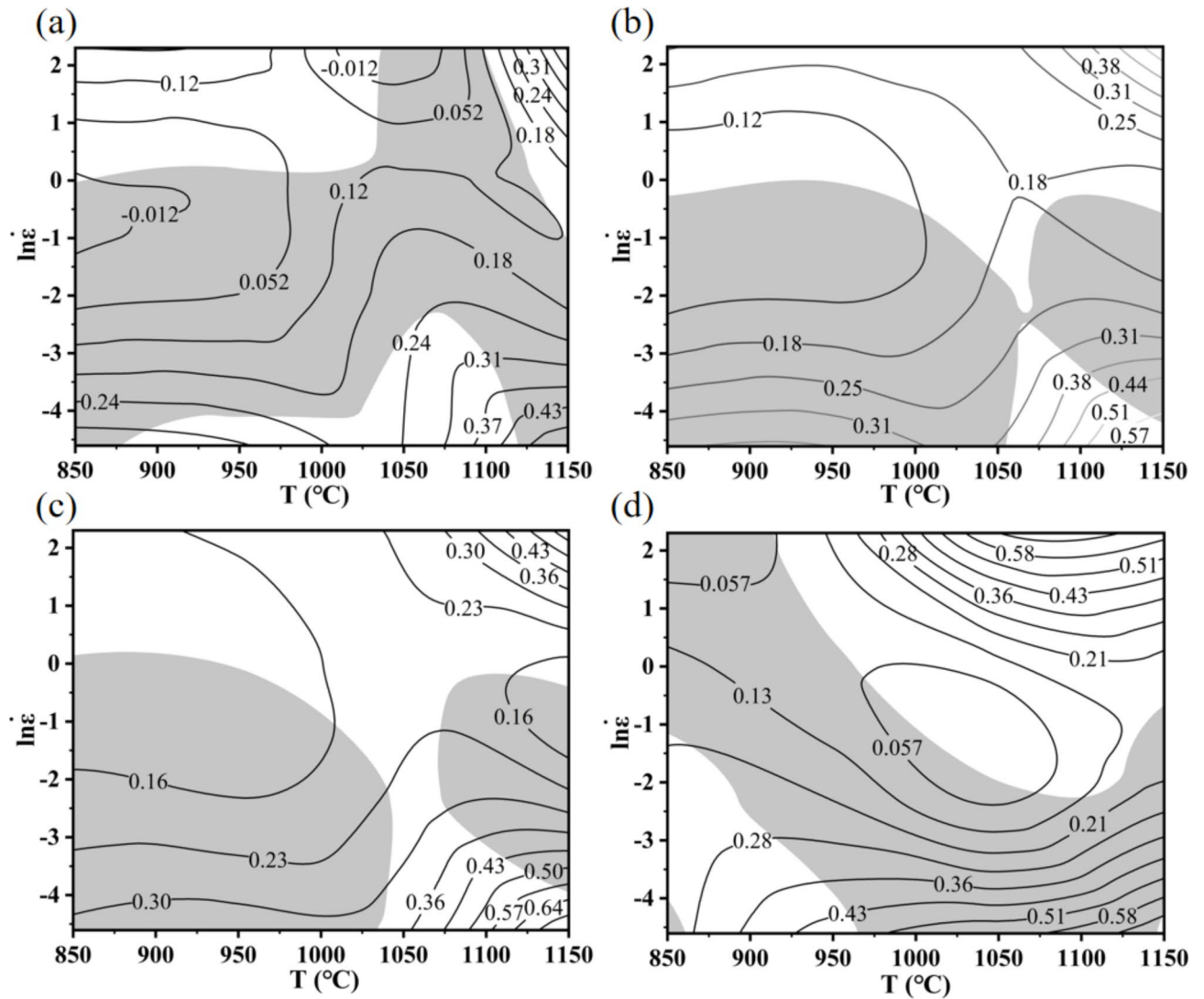
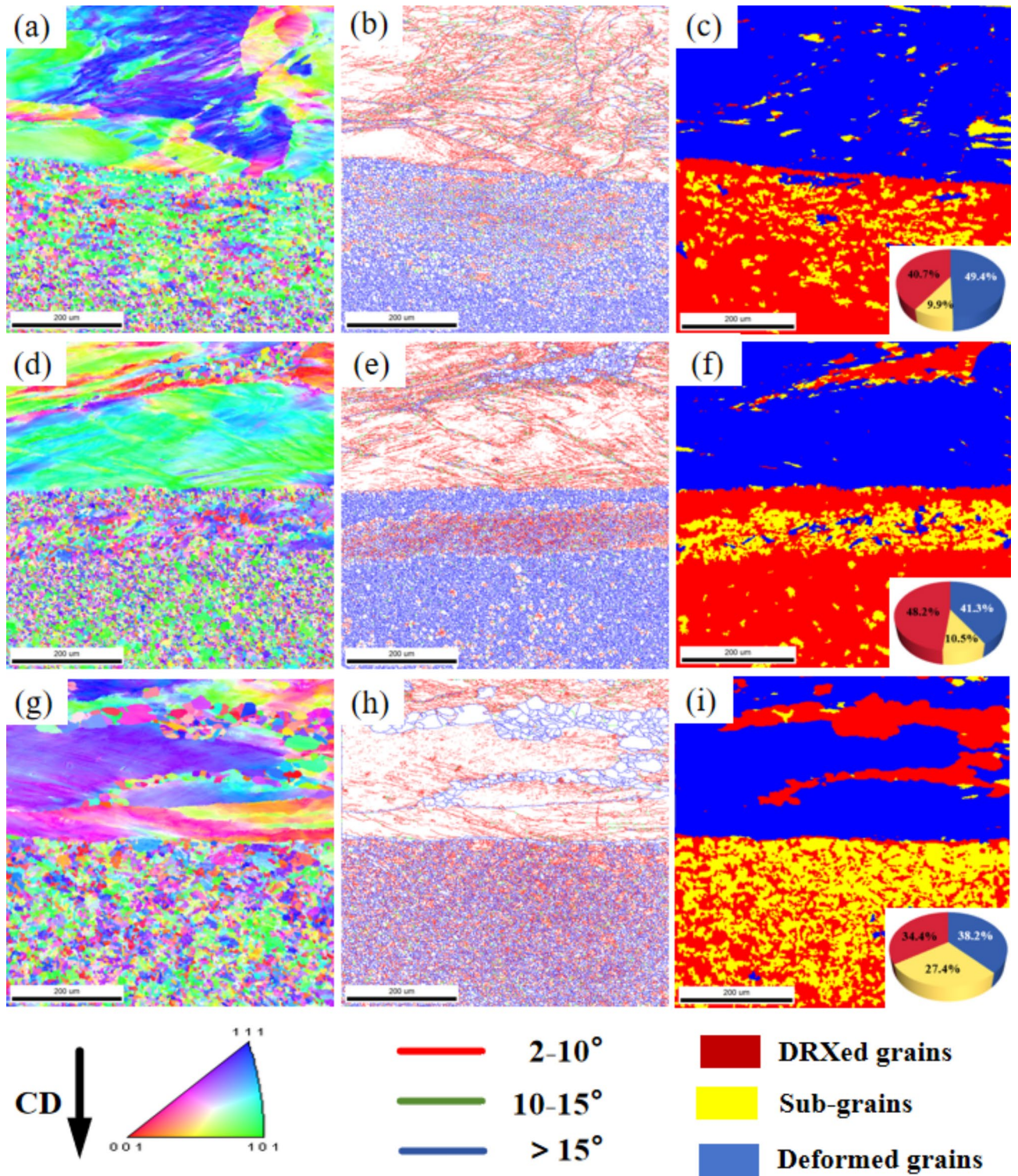


**Fig. 9.** Hot processing maps of Incoloy825/P110 bimetallic composite material at the strain of: (a) 0.1; (b) 0.3; (c) 0.5; (d) 0.7.

The machinable area of the thermal deformation diagram increases from 0.1 to 0.3 strain. When the strain is 0.1, the high strain rate ( $1-10 \text{ s}^{-1}$ ) in the unstable zone at temperatures of  $1030-1100 \text{ }^{\circ}\text{C}$  becomes a stable processing zone. The hot processing map of strain 0.3 is similar to that of strain 0.5, and the working area of high temperature and low strain rate increases. When the strain increases to 0.7, the stable processing area is concentrated in the low strain rate and low temperature region ( $0.01-0.1 \text{ s}^{-1}$ ,  $860-960 \text{ }^{\circ}\text{C}$ ). Because bimetallic composite materials cannot achieve the ideal state of uniform deformation within a short deformation time, it can lead to differences in deformation effects in different regions. According to the comprehensive hot processing diagrams, the safe range for hot processing of Incoloy825/P110 bimetallic composite materials is high strain rates ( $1-10 \text{ s}^{-1}$ ) at medium and high temperatures ( $925-1030 \text{ }^{\circ}\text{C}$  and  $1110-1150 \text{ }^{\circ}\text{C}$ ).

### Microstructural analysis

From load-bearing to energy dissipation, thermal stability, corrosion resistance, and damage resistance are ultimately included in the configuration of particles within the material<sup>42</sup>. As shown in Fig. 10, EBSD analysis was performed on the deformed microstructure of Incoloy825/P110 at room temperature to obtain the inverse pole figure (IPF), rotation angle boundary figure, and grain orientation diffusion figure (GOS) of the microstructure at different temperatures. Compared with Fig. 2, the original grains in Fig. 10a,d, and g show significant elongation along the compression direction. At  $950 \text{ }^{\circ}\text{C}/1 \text{ s}^{-1}$ , Incoloy825 has relatively few DRX grains. When the deformation temperature is low, the thermal motion of atoms is weak, and dislocation and grain boundary (BG) slip are more difficult. Therefore, the occurrence of DRX is difficult. By utilizing the temperature changes and softening behavior during deformation of alloys<sup>43</sup>, it can be demonstrated that temperature changes and strain rates have a significant impact on the thermal deformation behavior and mechanical properties of alloys in the microstructure.



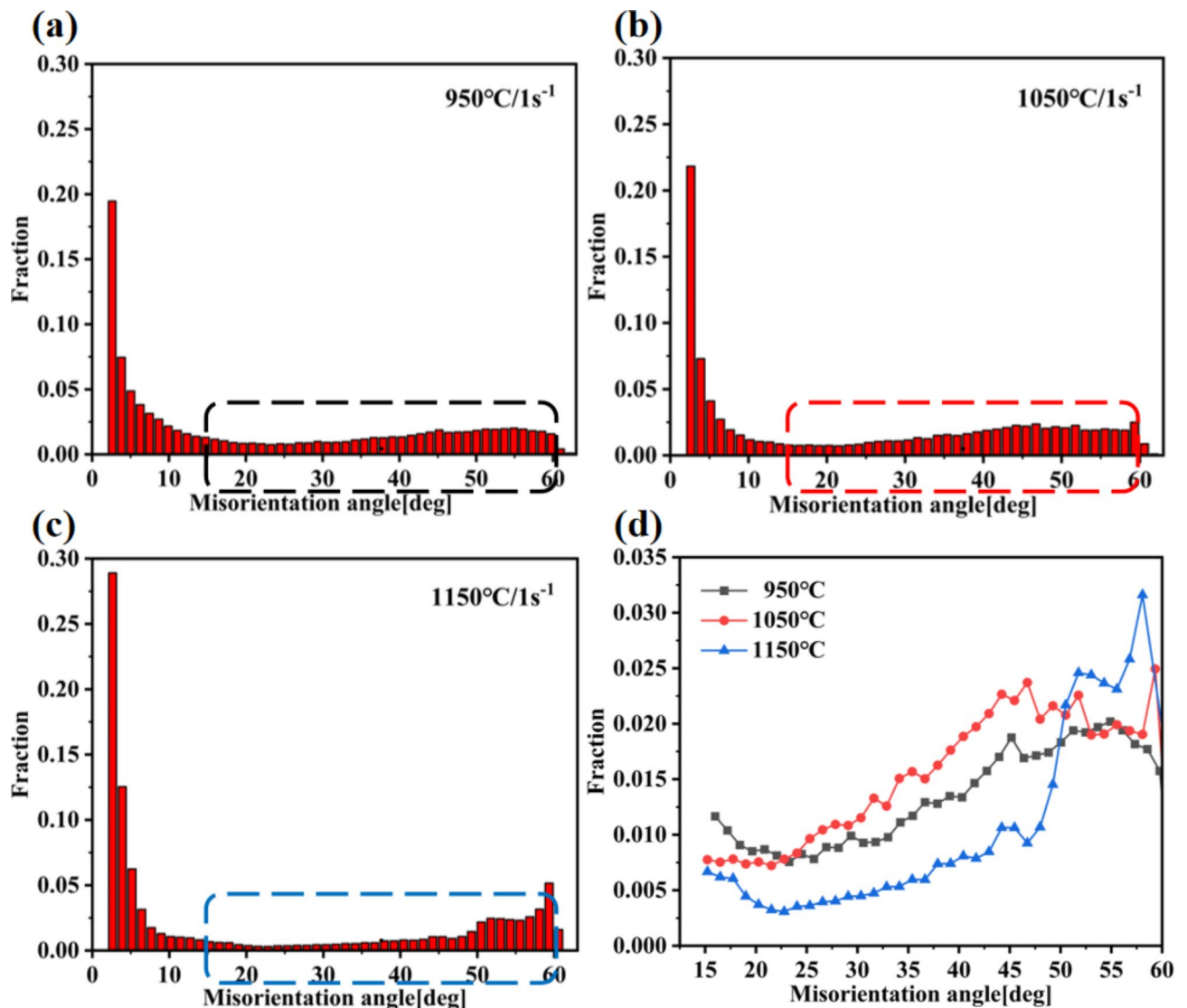
**Fig. 10.** EBSD post-treatment images of Incoloy825/P110 bimetallic composite materials at different temperatures: (a–c) 950 °C, (d–f) 1050 °C, (g–i) 1150 °C.

Figure 10b,e, and h, show angle grain boundaries at different temperatures. The red line represents low angle grain boundaries (LAGB,  $\theta \in (2^\circ, 10^\circ)$ ), the green line represents medium angle grain boundaries (MAGB,  $\theta \in (10^\circ, 15^\circ)$ ), and the blue line represents high angle grain boundaries (HAGB,  $\theta > 15^\circ$ ). There are a large number of LAGBs in the original grains after hot compression. During the hot compression process, when external pressure is initially applied, the difference in thermal expansion coefficients between Incoloy825 and P110 leads to noticeable thermal stress at the interface. This thermal stress facilitates the slip of atomic planes within the crystal structure. This process is accompanied by the generation and movement of dislocations. As

the compression increases, dislocations accumulate within the crystal and propagate through slip, leading to the potential superposition of multiple dislocations and ultimately forming dislocation sub-grain boundaries. When the temperature continues to rise to 1050 °C and 1150 °C, necklace-like structures appear<sup>44</sup>, enveloping the original deformed grains. In some cases, the original deformed grains may be covered by a large number of DRX grains.

The GOS method was used for statistical analysis of the volume fraction of DRX. The minimum angle was defined to categorize the grains into recrystallized grains (2°), sub-grains (5°), and deformed grains<sup>35</sup>, which correspond to the red, yellow, and blue regions in Fig. 10c,f, and i, respectively. The interface of Incoloy825/P110 bimetallic composite material shows a decrease in RDX grain proportion from 40.7 to 34.4% and deformation grain proportion from 49.4 to 38.2% with the increase of temperature, and a large number of sub-grains are generated. Further explanation shows that with the increase of temperature, dislocations in the crystal continuously accumulate and propagate through slip, leading to the potential superposition of multiple dislocations and ultimately forming low-energy dislocation walls or dislocation sub-grain boundaries.

To analyze the effect of thermal deformation on tissue at room temperature, EBSD data were analyzed in detail. As shown in Fig. 11, the grain boundary distribution trend of the sample at different temperatures is analyzed. It can be seen that the overall distribution of grain boundaries under different deformation conditions shows the same pattern, with a high proportion of LAGBs. Since MAGBs are predominantly derived from previously deformed austenite, they act as a reference for coherent phase transitions within this range. Thus, as shown in Fig. 11d, a comparison was made of MAGB at different temperatures. It can be seen that as the deformation temperature increases, the proportion of MAGBs increases and becomes larger.



**Fig. 11.** Misorientation angle distributions of Incoloy825/P110 bimetallic composite material under different temperatures: (a) 950 °C, (b) 1050 °C, (c) 1150 °C, (d) comparisons of large misorientation angle distributions.

During the hot deformation process of Incoloy825/P110 bimetallic composite material, DRX dominates the evolution of microstructure. In addition, it has a significant impact on its hot forming performance. Figure 12a–c show the Kernel Average Misorientation (KAM) map of Incoloy825/P110 hot deformed specimens at 950 °C, 1050 °C, and 1150 °C. Due to the crucial role of dislocation mobility in the nucleation process of DRX, KAM maps ( $\leq 5^\circ$ ) were used to study this process. KAM is related to dislocation density, where regions with high KAM can indicate the presence of a large number of dense dislocations related to deformation energy.

The KAM value is the indicator representing the net change in the dislocation density caused by plastic deformation. Statistical analysis of KAM values for Incoloy825 is shown in Fig. 12d–f. The average KAM values of the deformed Incoloy825 at temperatures of 950 °C, 1050 °C, and 1150 °C are 1.2406, 1.1962, and 0.8242, respectively. The KAM value of the deformed Incoloy825 decreases with increasing temperature. Statistical analysis of KAM values for P110 is shown in Fig. 12g–i. The average KAM values of the deformed P110 at temperatures of 950 °C, 1050 °C, and 1150 °C are 0.2948, 0.3532, and 1.1584, respectively. The KAM value of the deformed P110 increases with the increase of temperature. The deformed original grains in Incoloy825 contain a large number of dislocations, while the newly nucleated DRX grains have almost no dislocations, and the dislocations in P110 are almost the opposite. The interface position between two metal materials affects each other. The unit process of particle reconstruction in high-energy metastable states is usually more collective, accompanied by smaller displacement amplitudes<sup>45–47</sup>. It may also indicate that during thermal deformation, the microstructure and substructures at room temperature are transformed into each other through phase transition. When DRX occurs, most of the dislocations will be consumed. The local dislocations in the final organization include dislocations caused by phase transformation and substructures inherited from austenite deformation.

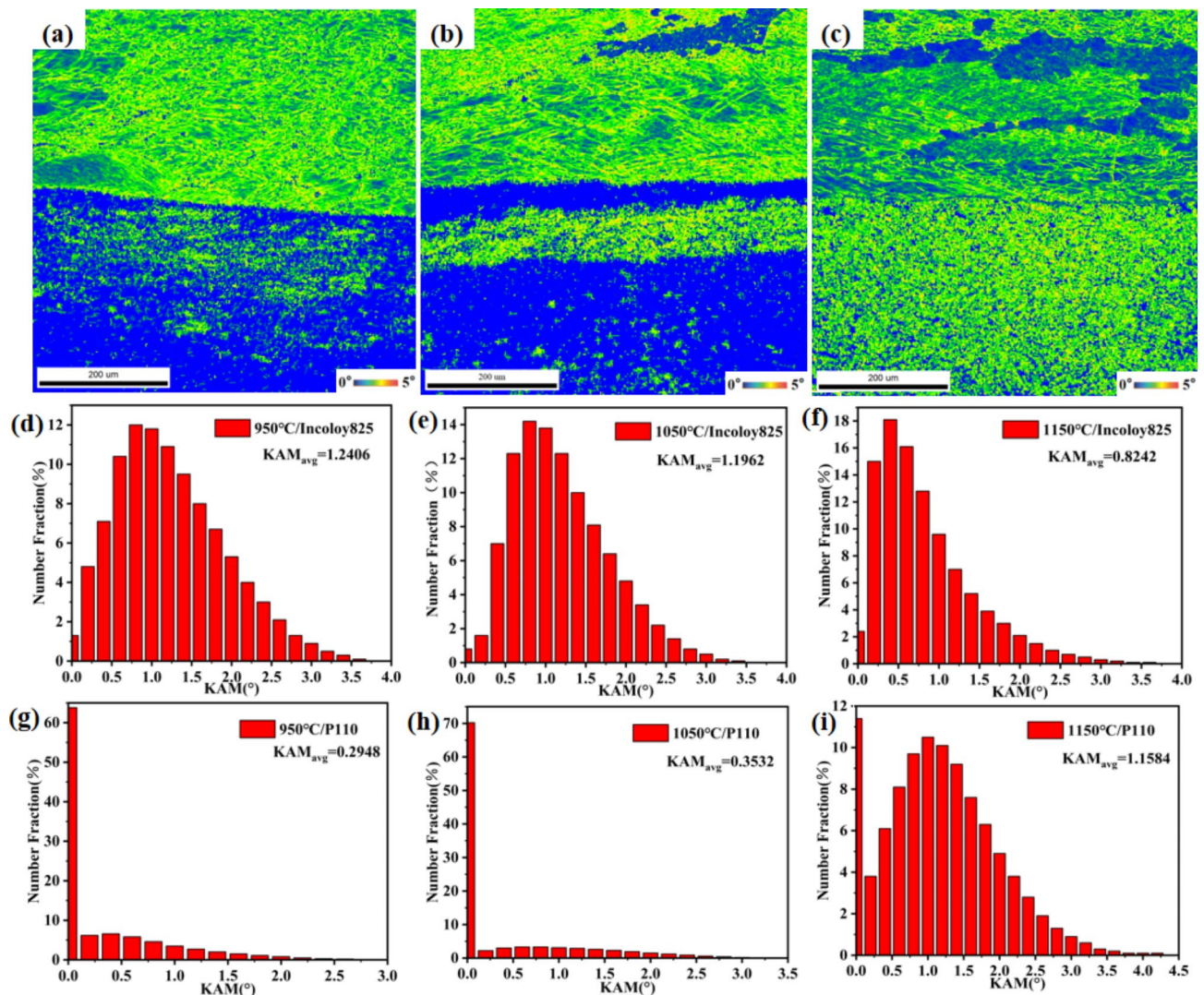


**Fig. 12.** (a) KAM distribution diagram at 950 °C corresponding to (d) Incoloy825 data analysis and (g) P110 data analysis, (b) KAM distribution diagram at 1050 °C corresponding to (e) Incoloy825 data analysis and (h) P110 data analysis, (c) KAM distribution diagram at 1150 °C corresponding to (f) Incoloy825 data analysis and (i) P110 data analysis.

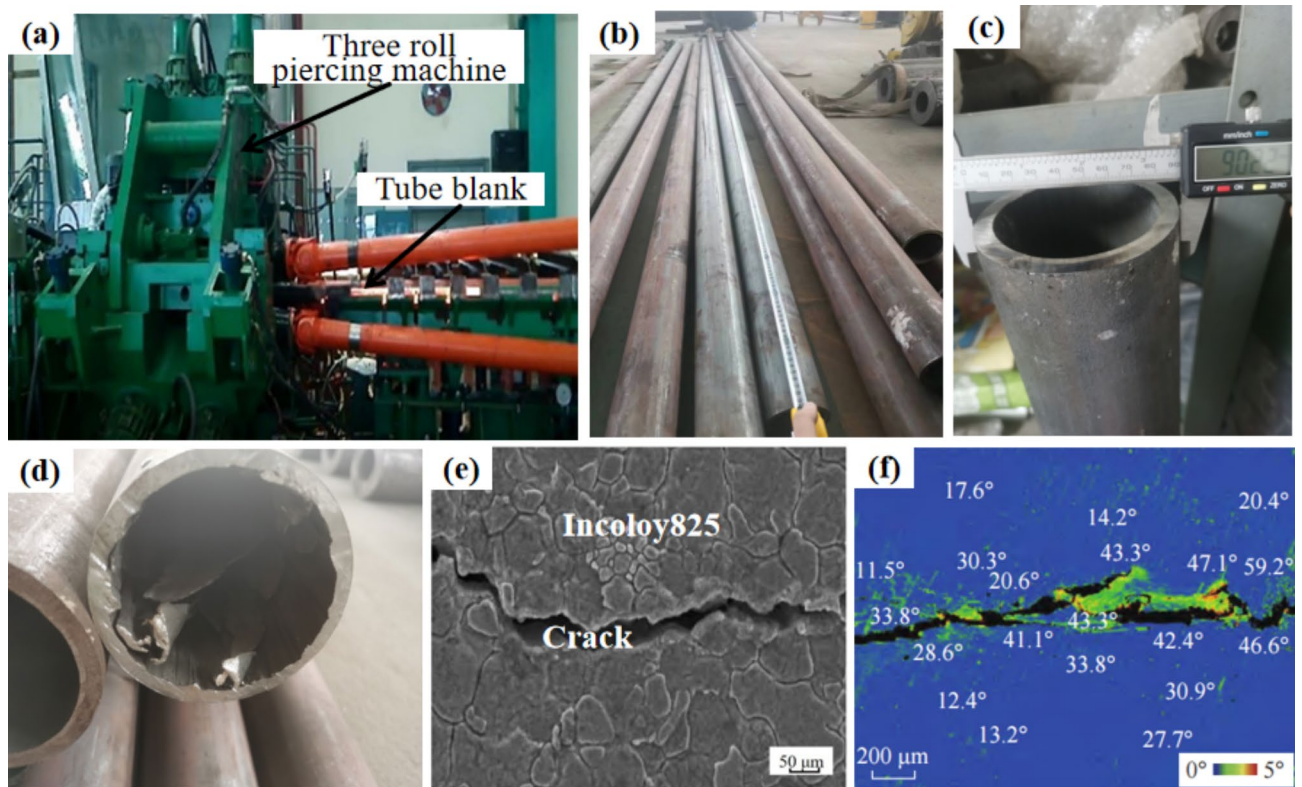


**Fig. 13.** Experiments on the Incoloy825/P110 bimetallic composite seamless pipe: (a) Perforation process diagram, (b) The length, (c) diameter, and (d) damage of the composite pipe, (e) Incoloy825 crack microstructure, (f) Stress distribution and grain boundary distribution of cracks.

### Perforation experiment of bimetallic composite seamless pipe

As illustrated in Fig. 13a, the Incoloy825/P110 bimetallic composite seamless pipe was manufactured by means of a three-roll piercing machine. As shown in Fig. 13b and c, within the safety range of the above hot processing, capillary tubes with lengths of approximately 5000 mm and  $\phi 90$  mm can be penetrated. However, when processed under parameters outside the machinable range, wrinkles and cracks appear in the capillary tube, as shown in Fig. 13d. The cracks are mainly concentrated in the liner pipe, as shown in Fig. 13e. Cracks occur at the grain boundaries of adjacent grains. For this multi-component and interface containing alloy, the stress distribution in the sample is not uniform due to the complexity of the local chemical and structural environment<sup>48</sup>. Cracks do not propagate smoothly under loading<sup>49</sup>, but exhibit intermittent patterns with platforms and steps. As shown in Fig. 12f, the deformation energy distribution near the crack can be observed from the crack KAM diagram, indicating significant stress-strain concentration at the crack initiation site. The grain boundary angle between adjacent grains at the crack location is above  $40^\circ$ . Therefore, during hot perforation forming, there is a significant concentration of stress and strain at large angle grain boundaries, which can lead to the formation and propagation of cracks.

### Conclusions

In order to study the properties of Incoloy825/P110 bimetallic composite seamless pipes, thermal deformation analysis was conducted on the pipe blank. This study conducted hot compression tests on Incoloy825/P110 bimetallic composite materials. The true stress-strain data was processed, analyzed, and modeled. The model was compensated and corrected, and a thermal processing map was established. The EBSD were employed for microstructure characterization and analysis. The thermal deformation behavior, microstructure evolution, and DRX mechanism of the composite material were studied. The study concluded that:

- (1) The rheological stress of Incoloy825/P110 bimetallic composite material increases with decreasing temperature or increasing strain rate. Establish constitutive equations for Arrhenius strain compensation and correction, and calculate AARE and R values of 4.94% and 0.9801, respectively. The results indicate that the established constitutive equation has high prediction accuracy for high-temperature rheological stress.
- (2) Based on the DMM model, a hot processing map for Incoloy825/P110 bimetallic composite materials has been constructed using the corrected stress-strain data. According to the comprehensive hot processing diagrams, the safe range for hot processing of Incoloy825/P110 bimetallic composite materials is high strain rates ( $1\text{--}10\text{ s}^{-1}$ ) at medium and high temperatures ( $925\text{--}1030\text{ }^\circ\text{C}$  and  $1110\text{--}1150\text{ }^\circ\text{C}$ ).

- (3) By analyzing the microstructure using EBSD, it can be found that DRX behavior has a significant impact on the thermal processing properties of composite materials. As the temperature increases, the proportion of DRX grains decreases from 40.7 to 34.4%, the proportion of deformed grains decreases from 49.4 to 38.2%, and a large number of sub-grains are generated. Further explanation shows that with the increase of temperature, dislocations in the crystal continuously accumulate and propagate through slip, ultimately forming dislocation sub-grain boundaries.

### Data availability

The data that support the findings of this study are available from the corresponding author upon reasonable request.

Received: 13 November 2024; Accepted: 9 January 2025

Published online: 19 January 2025

### References

- Liu, H. et al. Technology optimization analysis of three-roll rotary piercing process for seamless steel pipe. *JOM* **76**, 3465–3475 (2024).
- Li, S., Wei, Q., Shi, Y., Zhu, Z. & Zhang, D. Microstructure characteristics of inconel 625 superalloy manufactured by selective laser melting. *J. Mater. Sci. Technol.* **31**, 946–952 (2015).
- Dezfooli, M. S., Shamanian, M. & Golozar, M. A. The effect of bonding time on the microstructure and mechanical properties of dissimilar transient liquid phase bonding between UNS N08825 alloy and UNS S32750 super duplex stainless steel using the BNi-2 interlayer. *J. Manuf. Process.* **64**, 464–472 (2021).
- Rielli, V. V. et al. Effects of processing heterogeneities on the micro- to nanostructure strengthening mechanisms of an alloy 718 turbine disk. *Mater. Des.* **212**, 110295 (2021).
- Xiao, L. et al. Hot compression deformation behavior of novel Ni-based PM superalloy WZ-A3. *Rare Met. Mater. Eng.* **51**, 1427–1435 (2022).
- Chen, X.-M., Lin, Y. C., Wen, D.-X., Zhang, J.-L. & He, M. Dynamic recrystallization behavior of a typical nickel-based superalloy during hot deformation. *Mater. Des.* **57**, 568–577 (2014).
- Lu, Y. et al. Characteristic flow behaviour prediction and microstructure analysis of a commercial Si–Cr micro-alloyed spring steel under isothermal compression. *Vacuum* **186**, 110066 (2021).
- Chen, X.-M. et al. Characterization of hot deformation behavior and optimization of hot workability for GH4698 superalloy. *Mater. Charact.* **201**, 112916 (2023).
- Sun, B., Zhang, T. & Song, L. Flow behavior and dynamic recrystallization of a power metallurgy nickel-based superalloy during hot compression in ( $\gamma$  plus  $\gamma'$ )-phase region. *J. Alloys Compd.* **891**, 161944 (2022).
- Chen, X.-M. et al. An enhanced Johnson–Cook model for hot compressed A356 aluminum alloy. *Adv. Eng. Mater.* **23**, 2000704 (2021).
- Niu, L. et al. A modified Hansel–Spittel constitutive equation of Ti–6Al–4V during cogging process. *J. Alloys Compd.* **894**, 162387 (2022).
- Huang, X. et al. Constitutive relationships of 21–4 N heat-resistant steel for the hot forging process. *J. Mater. Res. Technol.* **9**, 13575–13593 (2020).
- Jenab, A., Sari Sarraf, I., Green, D. E., Rahmaan, T. & Worswick, M. J. The Use of genetic algorithm and neural network to predict rate-dependent tensile flow behaviour of AA5182-O sheets. *Mater. Des.* **94**, 262–273 (2016).
- Geng, P., Qin, G., Zhou, J. & Zou, Z. Hot deformation behavior and constitutive model of GH4169 superalloy for linear friction welding process. *J. Manuf. Process.* **32**, 469–481 (2018).
- Song, Y. et al. Hot deformation behavior and microstructural evolution of 2205 duplex stainless steel. *Mater. Res. Express* **7**, 046510 (2020).
- Zhao, G. et al. A comparative study of three constitutive models concerning thermo-mechanical behavior of Q345 steel during hot deformation. *Crystals* **12**, 1262 (2022).
- He, M., Yang, Y., Gao, F. & Fan, Y. Stress sensitivity origin of extended defects production under coupled irradiation and mechanical loading. *Acta Mater.* **248**, 118758 (2023).
- Zhang, S., Liu, C., Fan, Y., Yang, Y. & Guan, P. Soft-mode parameter as an indicator for the activation energy spectra in metallic glass. *J. Phys. Chem. Lett.* **11**, 2781–2787 (2020).
- Liu, C., Yan, X., Sharma, P. & Fan, Y. Unraveling the non-monotonic ageing of metallic glasses in the metastability-temperature space. *Comput. Mater. Sci.* **172**, 109347 (2020).
- Wang, Y. & Fan, Y. Incident velocity induced nonmonotonic aging of vapor-deposited polymer glasses. *J. Phys. Chem. B* **124**, 5740–5745 (2020).
- Prasad, Y. V. R. K. et al. Modeling of dynamic material behavior in hot deformation: Forging of Ti-6242. *Metall. Trans. A* **15**, 1883–1892 (1984).
- Chen, X. et al. Dynamic recrystallization and hot processing map of Ti–48Al–2Cr–2Nb alloy during the hot deformation. *Mater. Charact.* **179**, 111332 (2021).
- Tian, Y. et al. A systematic study on thermo-mechanical behavior, processing maps and recrystallization mechanism of Incoloy825 superalloy during hot compression. *J. Mater. Res. Technol.* **28**, 4551–4566 (2024).
- Kong, R. et al. Hot deformation behavior and microstructure evolution of Inconel 625 superalloy sheet. *J. Alloys Compd.* **915**, 165367 (2022).
- Chi, Z. et al. Failure behaviors and processing maps with failure domains for hot compression of a powder metallurgy Ni-based superalloy. *J. Mater. Res. Technol.* **20**, 3860–3874 (2022).
- Zhu, Y. et al. Three-dimensional hot processing map of a nickel-based superalloy (Alloy 925) established by modified artificial neural network model. *Intermetallics* **141**, 107433 (2022).
- Lin, X. et al. Establishment and validity verification of the hot processing map of a Ti–47.5Al–2.5V–1.0Cr–0.2Zr alloy with a lamellar microstructure. *Mater. Charact.* **183**, 111599 (2022).
- Chen, F. et al. Flow characteristics and intrinsic workability of IN718 superalloy. *Mater. Sci. Eng. A* **642**, 279–287 (2015).
- Chegini, M., Aboutalebi, M. R., Seyedein, S. H., Ebrahimi, G. R. & Jahazi, M. Study on hot deformation behavior of AISI 414 martensitic stainless steel using 3D processing map. *J. Manuf. Process.* **56**, 916–927 (2020).
- Li, X.-T., Tang, X.-Z., Fan, Y. & Guo, Y.-F. The interstitial emission mechanism in a vanadium-based alloy. *J. Nucl. Mater.* **533**, 152121 (2020).
- Wang, Y. et al. Predicting the energetics and kinetics of Cr atoms in Fe–Ni–Cr alloys via physics-based machine learning. *Scr. Mater.* **205**, 114177 (2021).

32. Jiang, L. et al. Deformation mechanisms in crystalline-amorphous high-entropy composite multilayers. *Mater. Sci. Eng. A* **848**, 143144 (2022).
33. Li, X.-T., Tang, X.-Z., Guo, Y.-F., Li, H. & Fan, Y. Modulating grain boundary-mediated plasticity of high-entropy alloys via chemo-mechanical coupling. *Acta Mater.* **258**, 119228 (2023).
34. Sellars, C. M. & McTegart, W. J. On the mechanism of hot deformation. *Acta Metall.* **14**, 1136–1138 (1966).
35. He, S., Li, C., Huang, Z. & Zheng, J. A modified constitutive model based on Arrhenius-type equation to predict the flow behavior of Fe–36% Ni Invar alloy. *J. Mater. Res.* **32**, 3831–3841 (2017).
36. Trimble, D. & O'Donnell, G. E. Constitutive modelling for elevated temperature flow behaviour of AA7075. *Mater. Des.* **76**, 150–168 (2015).
37. Zener, C. & Hollomon, J. H. Effect of strain rate upon plastic flow of steel. *J. Appl. Phys.* **15**, 22–32 (1944).
38. Prasad, Y. V. R. K. & Seshacharyulu, T. Processing maps for hot working of titanium alloys. *Mater. Sci. Eng. A* **243**, 82–88 (1998).
39. Prasad, Y. V. R. K. Processing maps: A status report. *J. Mater. Eng. Perform.* **12**, 638–645 (2003).
40. Zhang, B., Wang, Z., Yu, H. & Ning, Y. Microstructural origin and control mechanism of the mixed grain structure in Ni-based superalloys. *J. Alloys Compd.* **900**, 163515 (2022).
41. Tang, X.-Z. et al. Strain rate effect on dislocation climb mechanism via self-interstitials. *Mater. Sci. Eng. A Struct. Mater. Prop. Microstruct. Process.* **713**, 141–145 (2018).
42. Liu, C. et al. Concurrent prediction of metallic glasses' global energy and internal structural heterogeneity by interpretable machine learning. *Acta Mater.* **259**, 119281 (2023).
43. Wang, Y. et al. Atomistically informed mesoscale modelling of deformation behavior of bulk metallic glasses. *Acta Mater.* **276**, 120136 (2024).
44. Kumar, N., Owolabi, G. M., Jayaganthan, R. & Goel, S. Correlation of fracture toughness with microstructural features for ultrafine-grained 6082 Al alloy. *Fatigue Fract. Eng. Mater. Struct.* **41**, 1884–1899 (2018).
45. Bai, Z., Misra, A. & Fan, Y. Universal trend in the dynamic relaxations of tilted metastable grain boundaries during ultrafast thermal cycle. *Mater. Res. Lett.* **10**, 343–351 (2022).
46. Bai, Z., Balbus, G. H., Gianola, D. S. & Fan, Y. Mapping the kinetic evolution of metastable grain boundaries under non-equilibrium processing. *Acta Mater.* **200**, 328–337 (2020).
47. Wu, B., Bai, Z., Misra, A. & Fan, Y. Atomistic mechanism and probability determination of the cutting of Guinier–Preston zones by edge dislocations in dilute Al–Cu alloys. *Phys. Rev. Mater.* **4**, 020601 (2020).
48. He, M., Wang, Y. & Fan, Y. Metastable grain boundaries: the roles of structural and chemical disorders in their energetics, non-equilibrium kinetic evolution, and mechanical behaviors. *J. Phys. Condens. Matter* **36**, 343001 (2024).
49. Wang, Y. et al. Nonmonotonic effect of chemical heterogeneity on interfacial crack growth at high-angle grain boundaries in Fe–Ni–Cr alloys. *Phys. Rev. Mater.* **7**, 073606 (2023).

## Acknowledgements

(1) Central Government Guidance Fund for Local Science and Technology Development Project (YDZ-JSX20240054). (2) Shanxi Province Funding Project for Scientific Activities of Returned Overseas Students (20230032). (3) National Natural Science Foundation Joint Fund Project (U22A20188). (4) Shanxi Province Graduate Innovation Project (2024KY635). (5) Huai'an City's "Huai Talent Program" Innovation and Entrepreneurship Team for the Year 2022. (6) Demonstration Base for Joint Training of Graduate Students at Taiyuan University of Science and Technology (JD2022002). (7) The Fundamental Research Program (Free Exploration) Youth Project of Shanxi Province (202303021222171). (8) Taiyuan University of Science and Technology Scientific Research Initial Funding (20222136). (9) Excellent Doctoral Research Funding Project of Shanxi Province (20232060).

## Author contributions

The first two authors contributed equally to this work. All authors contributed to the study conception and design. Material preparation, data collection, and analysis were performed by L.h., G.hl, and L.q. The first draft of the manuscript was written by L.h., G.hl, and all authors commented on the current versions of the manuscript. All authors read and approved the final manuscript.

## Declarations

### Competing interests

The authors declare no competing interests.

### Additional information

**Correspondence** and requests for materials should be addressed to H.G.

**Reprints and permissions information** is available at [www.nature.com/reprints](http://www.nature.com/reprints).

**Publisher's note** Springer Nature remains neutral with regard to jurisdictional claims in published maps and institutional affiliations.

**Open Access** This article is licensed under a Creative Commons Attribution-NonCommercial-NoDerivatives 4.0 International License, which permits any non-commercial use, sharing, distribution and reproduction in any medium or format, as long as you give appropriate credit to the original author(s) and the source, provide a link to the Creative Commons licence, and indicate if you modified the licensed material. You do not have permission under this licence to share adapted material derived from this article or parts of it. The images or other third party material in this article are included in the article's Creative Commons licence, unless indicated otherwise in a credit line to the material. If material is not included in the article's Creative Commons licence and your intended use is not permitted by statutory regulation or exceeds the permitted use, you will need to obtain permission directly from the copyright holder. To view a copy of this licence, visit <http://creativecommons.org/licenses/by-nc-nd/4.0/>.

© The Author(s) 2025